Available online at www.sciencedirect.com

ScienceDirect

Ceramics International 42 (2016) 4507–4516

CERAMICS INTERNATIONAL

www.elsevier.com/locate/ceramint

Processing of ZrO_2 scaffolds coated by glass–ceramic derived from 45S5 bioglass

Franco M. Stábile[a], María P. Albano[a,*,1], Liliana B. Garrido[a], Cristina Volzone[a], Paulo Tambasco De Oliveira[b], Adalberto Luiz Rosa[b]

[a]*Centro de Tecnología de Recursos Minerales y Cerámica (CETMIC), CCT-La Plata CONICET, CICPBA, C.C. 49 (B1897ZCA) M. B. Gonnet, Provincia de Buenos Aires, Argentina*

[b]*School of Dentistry of Ribeirão Preto, University of São Paulo (FORP-USP), Avenue Do Café, s/n- Campus USP Monte Alegre, 14040-904, Ribeirão Preto, São Paulo, Brazil*

Received 9 September 2015; received in revised form 28 October 2015; accepted 25 November 2015
Available online 2 December 2015

Abstract

Three dimensional, highly porous, ZrO_2 scaffolds coated by glass–ceramic derived from 45S5 bioglass were fabricated. The surface reactivity of 45S5 in aqueous solution was investigated as a function of the immersion time. The influence of the solid loading on the rheological behavior of 45S5 aqueous slips with ammonium polyacrylate (NH_4PA) was studied; besides the effect of poly(vinyl)alcohol (PVA) on the relative viscosity was determined. The structure and microstructure of uncoated and coated ZrO_2 scaffolds were characterized. The high ionic exchange capability of 45S5 was demonstrated by the pH rise, the significant weight loss and the amorphous calcium phosphate nucleation, upon its immersion in aqueous solution. The addition of PVA did not affect the dispersion properties of the 45S5 powder, which were basically controlled by its negative surface charge. 30 wt% 45S5 slips with 4 wt% PVA exhibited a yield stress and an adequate viscosity in the low shear rate range, to produce a bioglass coating into the ZrO_2 scaffold. The glass-ceramic coating was distributed along the strut surfaces, forming a thin film without altering the porosity and the strut thickness of the original ZrO_2 scaffold structure.

Keywords: 45S5 bioglass; 45S5 surface reactivity; Rheological behavior; Glass–ceramic coated ZrO_2 scaffold; Scaffold structure

1. Introduction

Bioactive glasses are commonly used in form of particles or granules as bone substitute materials in orthopedic and dental applications [1,2]. The main drawback still impairing the use of bioactive glasses in load-bearing applications is their intrinsic brittleness. This aspect becomes even more critical when these materials are used in form of highly porous scaffolds, e. g. for bone tissue engineering applications, making very difficult their handling during surgical procedures and facing a high probability of failure after implantation. Therefore, the design of scaffolds for bone regeneration should be based on the criterion of optimizing their mechanical strength and biological compatibility.

3 mol% yttria- partially stabilized zirconia (Y-TZP) is used as a structural ceramic owing to its excellent mechanical properties [3]. Highly porous foams can be fabricated by a variety of processes [4,5]. Among them, the replication technique (also called the polymer-sponge method) produces porous ceramic structures that are similar to those of spongy bone [6]. Various bioactive glasses have been developed as bone replacement materials; however, the 45S5 bioglass discovered by Hench [1] is still taken as a standard glass composition. In this context, a porous ZrO_2 scaffold was chosen as a framework and the 45S5 bioglass was used as a coating layer to enhance the biocompatibility and osteoconductivity.

In order to achieve a continuous thin film of bioglass into the ZrO_2 scaffold, the bioglass aqueous surface reactivity and

*Corresponding author.
E-mail address: palbano@cetmic.unlp.edu.ar (M.P. Albano).
[1]Fax: +54 0221 471 0075.

http://dx.doi.org/10.1016/j.ceramint.2015.11.140
0272-8842/

the rheological behavior of aqueous 45S5 slips should be investigated. Successful colloidal processing of fine ceramic powders requires accurate control of both rheological properties and the state of the dispersion. Anionic polyelectrolytes such as NH_4PA are commonly used as dispersant of ceramic powders in aqueous media [7]. The polyelectrolyte adsorbs at the solid–liquid interface and infers repulsive force between the particles that keep them well dispersed; the repulsive interactions are caused by electrostatic and steric effects [8].

The preparation of stable suspensions in aqueous solution is strongly limited by the solubility of 45S5 bioglass, which is rather high in acidic conditions. In order to produce well-stabilized 45S5 slips, first its surface reactivity in an aqueous solution was investigated as a function of immersion time. The influence of the solid loading on the rheological behavior and viscosity of 45S5 aqueous slips stabilized with NH_4PA was studied. The binder is an essential component for the effective processing of films on substrates, it provides strong adhesion between the ceramic particles and the substrate, preventing the powder from detaching off the substrate during thermal treatment. PVA is frequently used in an aqueous media due to its affinity with the processing liquid [9]. Furthermore, it has an effective burnout profile without the formation of a deleterious residue. However, the addition of the organic binder may affect the rheology of the suspension [10]. Therefore, the influence of PVA addition on the relative viscosity of 30 wt% 45S5 suspensions stabilized with NH_4PA was investigated. Then, the 45S5 bioglass coating was achieved by infiltrating the ZrO_2 scaffold with an aqueous well-stabilized 45S5 slip with PVA. The structure and microstructure of uncoated and coated ZrO_2 scaffolds were characterized.

2. Experimental procedure

2.1. Raw materials and processing

A commercial 3 mol% yttria- partially stabilized zirconia (Y-TZP) (Saint-Gobain ZirPro, Chine, $d_{50}=0.64$ μm) was used to produce the scaffolds. The melt-derived 45S5 Bioglass powder (composition: 45 wt% SiO_2, 24.5 wt% CaO, 24.5 wt% Na_2O, 6 wt% P_2O_5; $d_{50}=5$ μm, $d_{95}<10$ μm) was used in this study. The details of the bioglass synthesis have been reported in a previous work [11].

A commercial ammonium polyacrylate solution (Duramax D 3500, Rohm & Haas, Philadelphia PA) and a 9 wt% PVA solution were used as deflocculant and binder, respectively. The degree of hydrolysis of PVA was 87–89% and the average molecular weight was in the range of 57,000– 66,000 g/mol.

A fully reticulated polyurethane foam was used as sacrificial template for the foam replication method. The foam was supplied in large samples and was cut into disks (12 mm in diameter and 3 mm in thickness).

The aqueous dissolution behavior of 45S5 was studied by measuring the pH of 20 wt% slips as a function of immersion time. Aqueous 45S5 slips with 0.20 wt% NH_4PA and different solid contents were prepared by suspending particles in deionized water via 40 min of ultrasound. In addition, 30 wt% suspensions with 0.20 wt% NH_4PA and two PVA concentrations were prepared.

For the impregnation of the disks, aqueous Y-TZP suspensions with a solid loading in the range 35–44 wt% were prepared by deagglomeration of the powder in distilled water with 0.11 wt% NH_4PA using an ultrasonic bath. Then, 6 wt% PVA was added to the slurry, followed by additional stirring. The pH of the suspensions was adjusted to 9.0 with ammonia (25 wt%). The disks were immersed in the above prepared slurry and centrifuged for 5 min at 2000 rpm. Then, they were manually retrieved from the Y-TZP suspension as quickly as possible, and the excess slurry was completely squeezed out. The disks were then dried at 100 °C for 24 h. The obtained Y-TZP bodies were heated to burn out the foam and binder at 800 °C for 5 h at a heating rate of 1 °C/min; finally they were sintered at 1500 °C for 2 h to obtain ZrO_2 scaffolds.

30 wt% aqueous 45S5 slurries with 0.20 wt% NH_4PA and 4 wt% PVA were prepared for the coating process. The fabricated Y-TZP scaffolds were immersed in the 45S5 slurry for 2 s, then they were manually withdrawn from the slurry at a constant velocity and dried at 100 °C for 24 h. The coated ZrO_2 scaffolds were sintered at 1100 °C for 1 h.

2.2. Characterization techniques

Dried 45S5 powders were characterized by differential thermal analysis (DTA) (STA 409, Netzsch Inc., Germany) at a heating rate of 10 °C/min in air. The infrared spectra (FTIR) of 45S5 powder after 3 days of immersion in water, and no reacted 45S5 powder were obtained with a spectrometer (Spectrum One Perkin Elmer) using a 4 cm^{-1} resolution over the 400–1300 cm^{-1} region. The weight loss of 45S5 powder after immersion during 3 days was measured. Zeta potential against pH curves were determined with an instrument Zetasizer nano ZS (Malvern Instruments, UK) for 0.05 vol% slips of 45S5 with 0.20 wt% NH_4PA and without NH_4PA in the pH range of 6–10.5. The pH adjustment was achieved with HCl or NH_4OH solutions. The pH was measured with a pH meter calibrated with buffer solutions (pH 4, 7 and 10, Merck, Germany).

Steady state flow curves of 45S5 slips were performed by measuring the steady shear stress value as a function of shear rate in the range of 0.5 to 542 s^{-1} using a concentric cylinder viscometer (Haake VT550, Germany) at 25 °C. A coaxial cylinder system with two gaps (sensor system NV Haake) was used. As soon as stationary conditions were reached at each shear rate, the shear rate increased in steps up to the maximum value and then decreased. The relative viscosity $\eta_r=\eta_s/\eta_f$, where η_s and η_f are the viscosities of the suspension and the fluid medium (PVA+water+dispersant), respectively, was measured for 30 wt% slips with 0.20 wt% NH_4PA and two PVA concentrations.

The density of the scaffolds (ρ_s) was determined from the mass and dimensions of the sintered bodies. The total porosity P was then calculated by:

$$P=1-\rho_s/\rho_z=1-\rho_{relative} \quad (1)$$

where $\rho_z=6.05$ g/cm^3 is the theoretical density of Y-TZP.

The total porosity of coated samples was calculated by the modified relationship:

$$P = (1 - \rho_s/\rho_z - \rho_{cm}/\rho_{ct}) \times 100 \quad (2)$$

where ρ_{cm} is the coating density calculated for each sample as:

$$\rho_{cm} = w_f - w_i/V \quad (3)$$

w_i and w_f are respectively the weight of the scaffold before and after coating and V is the scaffold's volume; ρ_{ct} is the theoretical coating density ($\rho_{bioglass} = 2.7$ g/cm^3).

The microstructure of the scaffolds was characterized using scanning electron microscopy (SEM) (FEI Quanta 200 MK2 Serie), energy dispersive X-ray analysis (EDXA) and micro-computed tomography (micro-CT, SkyScan 1172, Belgium). The determination of the pore size of uncoated and coated scaffolds was carried out with the micro-CT. The strut thickness of the scaffolds were measured by SEM; in order to obtain a strut thickness distribution, more than 250 struts were measured from different images.

3. Results and discussion

3.1. Characterization and surface reactivity of 45S5 powder

Fig. 1 shows the pH as a function of the immersion time for 20 wt% 45S5 slips. An important increase in pH during the first minutes of immersion in aqueous solution from 7.7 (the initial pH of water) to 11.6 was found. After that, the pH stayed nearly constant over the remaining 3 days of the experiment.

Silicate glasses are a collection of silica tetrahedral connected by Si–O–Si binding oxygen bonds [2]. Silicon is therefore the glass network forming atom, sodium and calcium are network modifiers that disrupt the network by forming non-bridging oxygen bonds such as Si–O$^-$ Na$^+$/Ca^{2+} bonds [12]. The immersion of the glass in water produces a rapid cation exchange of Ca^{2+} and Na^+ with H^+ from the solution, creating silanol bonds (Si–OH) on the glass surface and increasing the OH^- concentration. Thus, the pH rise upon the 45S5 immersion in the aqueous solution could be explained by the following ion exchange reaction on the glass surface:

$$Si-O^-Na^+ + H^+ + OH^- \rightarrow Si-OH + Na^+(aq.) + OH^- \quad (4)$$

A similar exchange reaction occurrs for Ca^{2+}. The pH of the solution increases and a silica-rich (cation-depleted) region forms near the glass surface [2,13]. After the initial rapid Ca^{2+},Na^+ /H^+ exchange reaction, the 45S5 dissolution rate decreased (lower slope of the pH vs. immersion time curve, Fig. 1) as a consequence of the lower H^+ concentration in solution (pH 11.6–11.8).

The glass also releases phosphate to the solution; according to an NMR study [14], the phosphorous is present in an orthophosphate environment, with charge balanced by sodium and or/calcium without any P–O–Si bonds. The phosphorous is therefore isolated from the silica network and removes sodium and calcium cations from their network-modifyng role [15]. This explains why phosphate is rapidly lost from the glass on exposure to aqueous environment [16].

Fig. 2 shows the FTIR spectra of the unreacted 45S5 powder and after immersion in aqueous solution for 3 days. The bands for 45S5 glass before immersion (unreacted) were due to Si–O vibrational modes: Si–O–Si bend at about 470 cm^{-1}, Si–O$^-$ alkali$^+$ stretch NBO (non-bridging oxygens) at about 920 cm^{-1} and Si–O–Si stretch at about 1030 cm^{-1}. After immersion in aqueous solution for 3 days the spectrum showed the following changes: disappearance of the NBO band at 920 cm^{-1} and Si–O–Si stretch band at about 1030 cm^{-1}, and appearance of a shoulder at approximately 570 cm^{-1}. This is the most characteristic region for apatite and other phosphates; it corresponds to P–O bonding vibrations in a PO_4^{3-} tetrahedron [17,18]. A shoulder in this region indicated the presence of amorphous calcium phosphate. Thus, the FTIR results suggested the nucleation of amorphous calcium phosphate on the 45S5 surface upon its immersion in water for 3 days.

Soda-lime phosphosilicate-based bioactive glasses are well known to form an hydroxycarbonate apatite (HCA) layer upon immersion in simulated body fluid (SBF). Hench et al. [19]

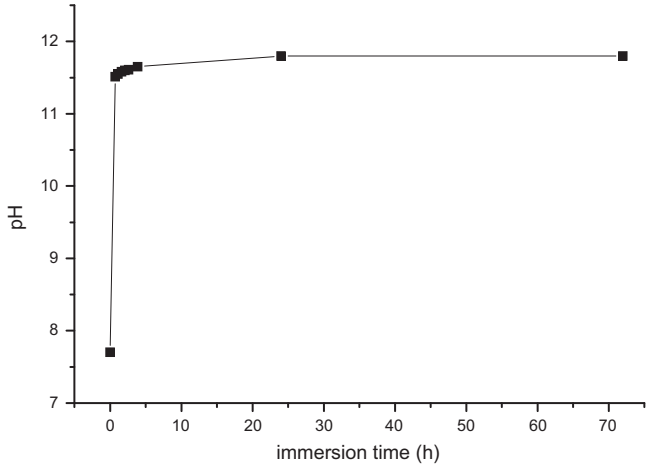

Fig. 1. pH as a function of the immersion time for 20 wt% 45S5 slips.

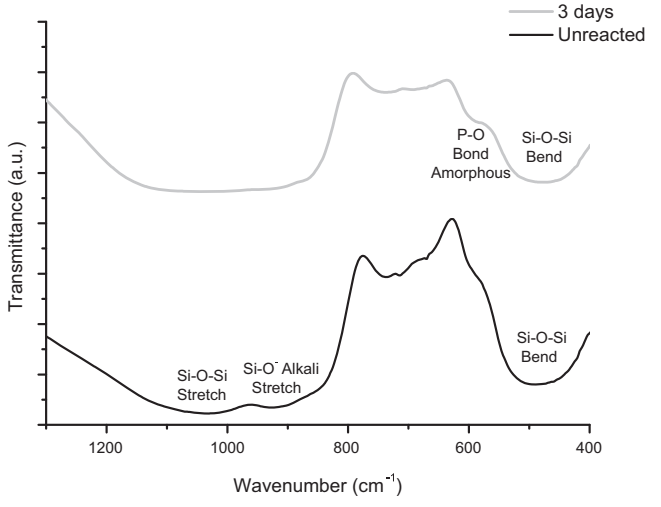

Fig. 2. FTIR spectra of the unreacted 45S5 powder and after 3 days of immersion in aqueous solution.

proposed five reaction steps for HCA formation in SBF as follows:

Step 1: Rapid exchange of cations such as Na^+ and Ca^{2+} with H^+ from solution (Eq. (4)).
Step 2: Attack of the silica glass network by OH^-, breaking Si–O–Si bonds. Soluble silica is lost in the form of $Si(OH)_4$ to the solution, leaving more Si–OH (silanols) at the glass solution interface:

$$Si-O-Si+H_2O \rightarrow Si-OH+OH-Si \quad (5)$$

Step 3: Condensation of Si–OH groups near the glass surface; and repolymerization of the SiO_2 -rich layer on the surface depleted of alkali and alkali earth cations:

$$HO-Si-OH+HO-Si-OH \rightarrow HO-Si-O-Si-OH+H_2O \quad (6)$$

Step 4: Migration of Ca^{2+} and PO_4^{3-} groups from solution to the surface, forming calcium-phosphate clusters on the SiO_2 -rich layer, followed by growth of amorphous calcium-phosphate.
Step 5: Incorporation of OH^- and CO_3^{2-} from solution and crystallization of the amorphous calcium-phosphate film to HCA.

In this study, the amorphous calcium phosphate formation could be interpreted by the above mechanism. Although under the present experimental conditions HCA was not detected, the first four steps of the bio-mineralization mechanism proposed by Hench [19] have likely occurred. Cerruti et al. [20] also found that 45S5 bioglass formed a Ca–P layer upon immersion in water.

The considerably high weight loss (37 wt%) of 45S5 after immersion in aqueous solution for 3 days together with the pH rise observed (Fig. 1) are strong evidence of its high ionic exchange capability. Glass composition is the variable that has the greatest influence on its dissolution rate [2]. The silica tetrahedron and its associated bonds can be described by Q^n notation, where n is the number of bridging oxygen bonds. An NMR study [21] showed that 45S5 bioglass primarily consists of 69% chains and rings of Q^2, with 31% of Q^3 units providing some cross-linking. Thus, the low proportion of bridging oxygen bonds for 45S5 glass results in a less connected network, which is more prone to dissolution, and therefore the stages of the Hench's mechanism listed above happen more rapidly [2].

The aqueous dissolution of 45S5 powder produced a pH rise with a simultaneous increase in Ca^{2+}, Na^+ and PO_4^{3-} ions concentrations, inducing calcium phosphate nucleation. Calcium phosphate is found to nucleate on the Si–OH groups, which have a negative charge in solution [22]. The released Ca^{2+} and PO_4^{3-} ions accelerate calcium phosphate nucleation by increasing its ionic product which became higher than that of K_{sp}. Once the calcium phosphate nuclei are formed at the glass surface, they can grow spontaneously by consuming the calcium and phosphate ions in the aqueous solution.

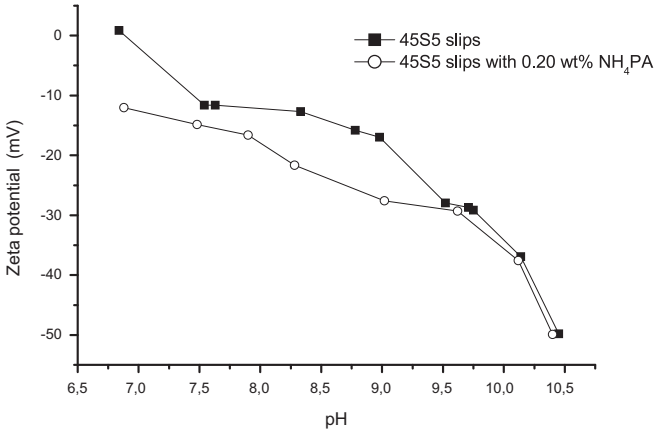

Fig. 3. Zeta potential versus pH curves of 45S5 slips with 0 and 0.20 wt% NH_4PA.

Fig. 3 shows the zeta potential versus pH curves of 45S5 slips with 0 and 0.20 wt% NH_4PA. The isoelectric point (IEP) of the 45S5 powder was at about pH 6.8. The Ca^{2+} ions interacted with the negatively charged phosphate ions in the aqueous solution resulting in the nucleation of amorphous calcium phosphate (low Ca/P ratio, [22]) at the 45S5 surface, and imparting a low negative surface charge at about pH 7 (Fig. 3).

The calcium phosphate surface consists of two distinct surface groups $\equiv CaOH_2^+$ and $\equiv PO^-$ [23]. The Ca sites loss a proton in strongly alkaline solutions according to the following reaction:

$$\equiv CaOH_2^+ \rightarrow \equiv CaOH^0+H^+ \quad (7)$$

The $\equiv CaOH_2^+$ concentration decreases with increasing pH and at pH > 9.5 the $\equiv CaOH^0$ sites predominate [23]. As a consequence, the negative zeta potential of 45S5 powder significantly increased at pH > 9.5 (Fig. 3). The addition of NH_4PA increased the negative surface charge of the powder in the pH range 6.8–9.4; at pH 9.5 the negative zeta potential values of 45S5 slips with and without NH_4PA were nearly the same (approximately −30 mV, Fig. 3).

The ammonium polyacrylate dissociation according to the reaction:

$$RCOONH_4 \rightarrow RCOO^- + NH_4^+ \quad (8)$$

begins at pH > 3.5; at pH values ≥ 8.5 the polymer charge is negative with the degree of ionization approaching 1 [24]. The $RCOO^-$ groups of the polyelectrolyte fully dissociated at pH ≥ 9.5 were absorbed at some of the positive 45S5 surface groups. However, as the amount of positive sites on the 45S5 surface decreased with increasing pH, the powder had less positive groups at which the $RCOO^-$ could be adsorbed. The low adsorption of NH_4PA on the $_4$5S5 powder at pH ≥ 9.5 did not increase significantly its negative surface charge. Consequently similar negative zeta potential values were found for 45S5 slips with and without NH_4PA at pH ≥ 9.5.

In order to investigate the chemical and physical transformations of 45S5 during sintering, its DTA analysis was carried out; the DTA curve of the bioglass is shown in Fig. 4. Five thermal events were detected at 112, 550, 659, 1209 and 1243 °C, which

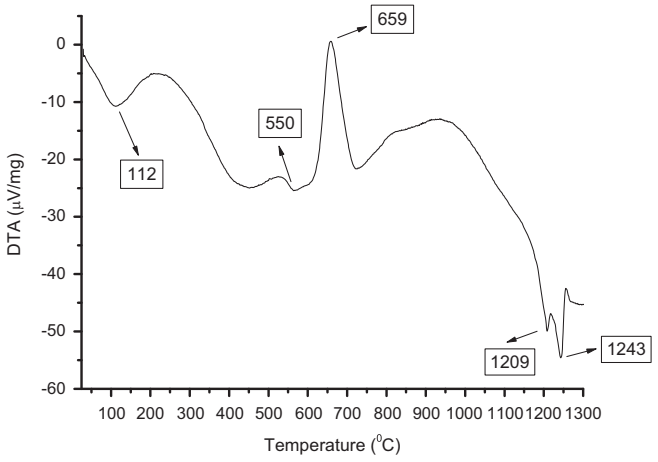

Fig. 4. DTA analysis of 45S5 powder.

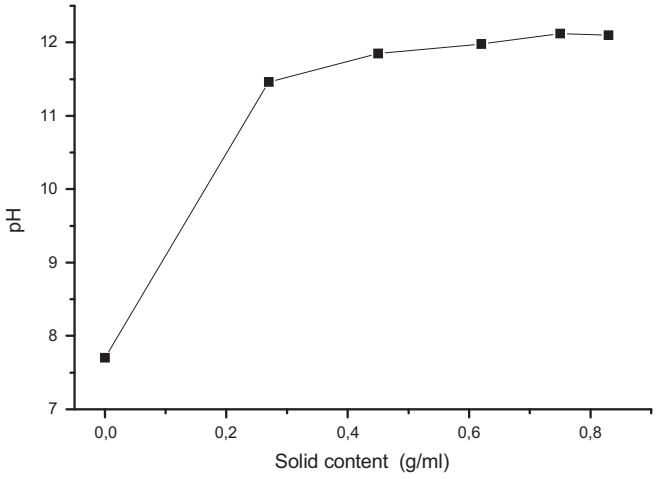

Fig. 5. Variation of pH with increasing the solid content from 0 to 0.8 g/ml (30 wt%) 45S5.

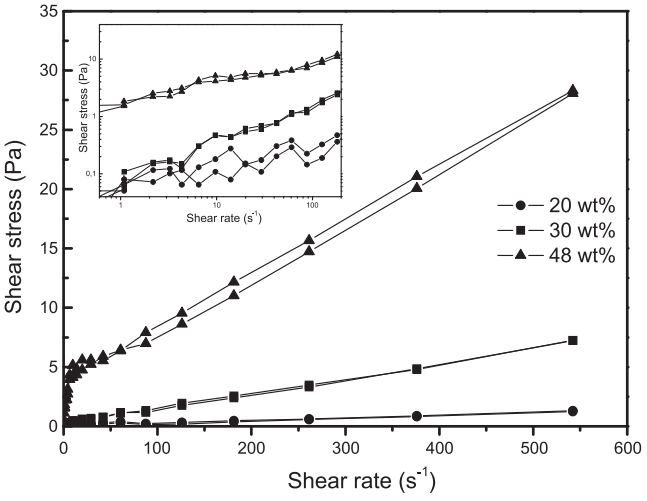

Fig. 6. Flow curves of shear stress versus shear rate for 45S5 slips with 0.20 wt% NH_4PA and different solid loading at pH 12. In the insert, the flow curves of the slips at low shear rates are shown in a log–log scale to observe more clearly the differences among them.

corresponded to the water loss, glass transition temperature, glass crystallization and fusion of two different crystalline phases, respectively. A previous XRD study [25] revealed that the crystalline phases were $Na_2CaSi_2O_6$ and $NaCaPO_4$.

3.2. Rheological properties

During the aqueous colloidal processing of 30 wt% 45S5 slips with 0.20 wt% NH_4PA, the variation of pH with increasing the solid content from 0 to 0.8 g/ml (30 wt%) was measured (Fig. 5). The addition of 0.25 g/ml of the glass (which corresponded to 20 wt% 45S5, Fig. 1) to an aqueous solution with NH_4PA produced a pH rise from 7.7 to 11.5, a lesser increase in pH with further increasing the solid content up to 0.8 g/ml was found (lower slope of the pH vs. solid content curve). The Na^+, Ca^{2+}/H^+ exchange reaction at the glass solution interface was responsible for the significant increase in pH with the addition of 0.25 g/ml 45S5. For greater concentrations of 45S5 in the range 0.25–0.8 g/ml, the accumulation of OH^- in the solution (low H^+ concentration) markedly reduced the exchange reaction rate (Eq. (4)), reaching a pH value of 12 for 0.8 g/ml 45S5.

Fig. 6 shows the flow curves of shear stress versus shear rate for 45S5 slips with 0.20 wt% NH_4PA and different solid loading at pH 12. Since the dip coating process is performed in the low shear rate range, the flow curves of the suspensions at low shear rates are shown in a log–log scale to observe more clearly the differences among them (see the insert in Fig. 6). The 20 wt% 45S5 slip exhibited a nearly Newtonian behavior (yield stress ≈ 0.086 Pa) and a viscosity value of 2.0 mPa.s in the low shear rate range. The 20 wt% suspension was dominated by repulsive forces; thus, it was stabilized. The low adsorption of the negatively charged polyelectrolyte at pH ≥ 9.5 did not contribute significantly to an increase of the negative zeta potential of the 45S5 powder (NH_4PA-adsorbed 45S5 particles) (Fig. 3). Thus, the dispersion properties of 20 wt% 45S5 slips with NH_4PA at pH 12 was basically controlled by the 45S5 powder surface charge. The high negative zeta potential of the 45S5 powder at pH ≥ 9.5 (Fig. 3) resulted in well dispersed slip with a low viscosity value. Flocculation due to the presence of free polymer in the solution was not observed at low solid loading (20 wt%).

The flow curves of 30 and 48 wt% 45S5 slips, both in the low and in the whole shear rate range studied, were satisfactorily fitted with the Bingham plastic model. The Bingham model equation is:

$$\tau = \tau_0 + \eta_p \dot{\gamma} \quad (9)$$

where τ is the shear stress, $\dot{\gamma}$ is the shear rate, τ_0 is the yield stress and η_p represents the limiting viscosity at a high shear rate range. The particles in a flocculated suspension form flocs because of the mutual attraction between particles, and the yield value τ_0 of the model is a parameter that indicates the degree of aggregation and consequently the slip flocculation [26]. The rheological parameters of the model in the low shear rate range were: $\tau_0 = 0.170$ Pa, $\eta_p = 13.7$ mPa.s for 30 wt% slips; and $\tau_0 = 2.453$ Pa, $\eta_p = 58.0$ mPa.s for 48 wt% slips. The low τ_0 values indicated weak flocculation; τ_0 and the slip viscosity markedly increased with increasing the solid content from 30 to

48 wt%. The increase in the solid content increased the OH^- and cations concentrations in the aqueous solution (Eq. (4), Fig. 5). The increase in the ionic strength due to the presence of a large amount of ions and free polymer in solution decreased the negative surface charge of 45S5 powder due to the large compression of the double layer [27]; as a consequence an increase in τ_0 and viscosity with increasing the solid content was found.

As we have mentioned, the addition of PVA was necessary for an effective processing of films on substrates. However, PVA can change the rheology of a stabilized suspension. Fig. 7a shows the flow curves of shear stress versus shear rate for 30 wt% 45S5 slips with 0.20 wt% NH_4PA and different PVA contents: 0, 1 and 4 wt%; in the insert, the flow curves of the slips at low shear rates are represented in a log-log scale. An adequate slip to produce a coating must be fluid to penetrate into the structure and also presents enough viscosity in the low shear rate range. Thus, coating slips having a shear thinning behavior with yield stress and enough viscosity may lead to an optimized coating [28]. The flow curves of 30 wt% slips with 1 and 4 wt% PVA, both in the low and in the whole shear rate studied, were satisfactorily fitted with the Bingham plastic model; they exhibited a yield stress followed by a nearly Newtonian flow. In the regime of low shear rates as proceeds in the dip coating process, higher yield stress and viscosity values were found for the slips with 4 wt% PVA ($\tau_0 = 1.480$ Pa; $\eta_p = 25.7$ mPa.s) with respect to those for the slips with 1 wt% PVA ($\tau_0 = 0.800$ Pa; $\eta_p = 15.0$ mPa.s). 30 wt% 45S5 slips with 4 wt% PVA exhibited a yield stress and an adequate viscosity in the low shear rate range, to produce a bioglass coating into the ZrO_2 scaffold.

The flow curves for the fluid part of 30 wt% slips with 1 and 4 wt% PVA are shown in Fig. 7b. The fluids were Newtonian; an increase in the PVA content from 1 to 4 wt% resulted in a more viscous fluid phase which increased the slip viscosity (Fig. 7a and b). Thus, the curves indicated that the differences in the slip viscosity were merely due to the differences in the viscosity of the fluid part. Fig. 8 represents the relative viscosity at different shear rates for 30 wt% 45S5 slips with 0.20 wt% NH_4PA and different PVA contents. Almost the same relative viscosities at high shear rates were found for different PVA contents. This indicated that the degree of slip dispersion was nearly the same irrespective of the PVA content. Thus, the PVA did not affect the dispersion properties of the 45S5 powder, which were basically controlled by its negative surface charge.

3.3. Scaffolds structure

Fig. 9 shows the porosity change of the ZrO_2 scaffolds as a function of the aqueous ZrO_2 slip concentration. The porosity of the scaffolds increased from 80 to 93% with decreasing the ZrO_2 slip concentration from 44 to 35 wt%, respectively. The scaffolds with an extremely high porosity of 93% were fragile to hand; on the other hand, some pores were observed to be partly blocked when the porosity of the ZrO_2 scaffold was

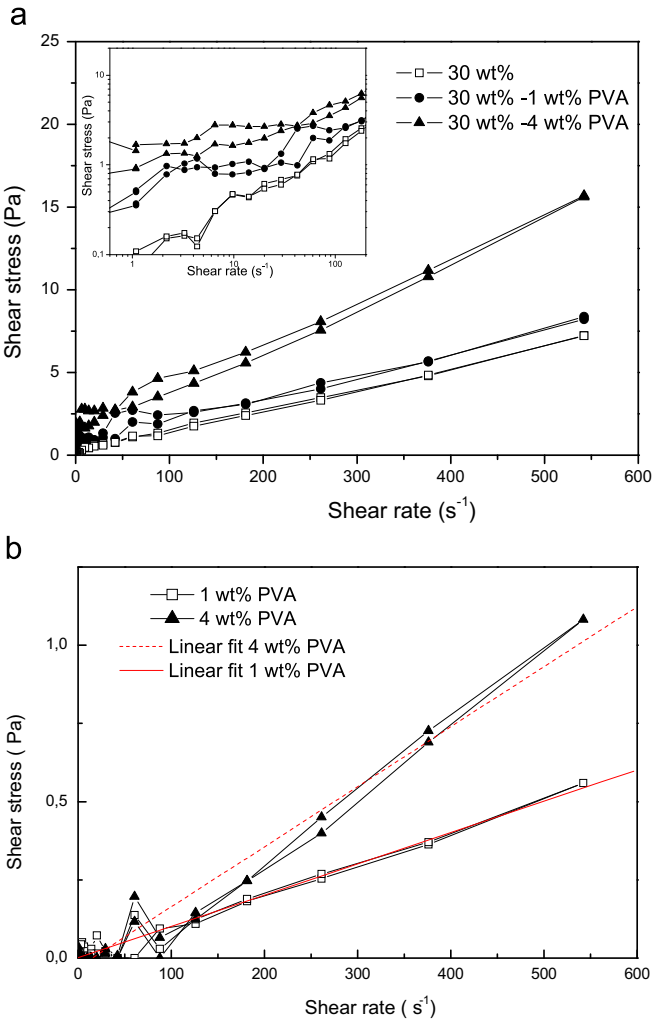

Fig. 7. Flow curves of shear stress versus shear rate for: (a) slips and (b) fluid part, of 30 wt% 45S5 slips with 0.20 wt% NH_4PA and different PVA contents. In the insert, the flow curves of the slips at low shear rates are represented in a log–log scale.

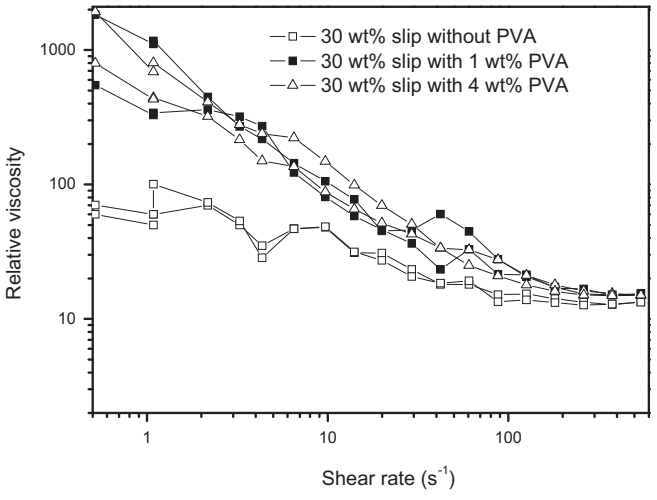

Fig. 8. Relative viscosity at different shear rates for 30 wt% 45S5 slips with 0.20 wt% NH_4PA and different PVA contents.

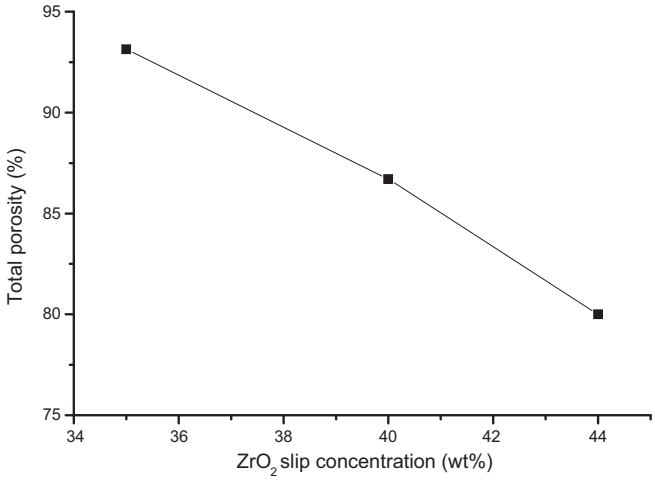

Fig. 9. Total porosity of the ZrO_2 scaffolds as a function of the aqueous ZrO_2 slip concentration.

reduced to 80%. Consequently, the scaffolds with 87%, prepared from 40 wt% slips, were selected to be coated with a bioglass surface layer. Based on these results, the scaffold porosity was controlled by changing the aqueous ZrO_2 slip concentration.

Fig. 10a shows a SEM image of the ZrO_2 scaffold with 87% porosity. The ZrO_2 scaffold exhibited a well-developed open macropore structure; the majority of the pores were open, whereas only a few ones were blocked or closed. The porosity values obtained by micro-CT analysis for the uncoated and coated ZrO_2 scaffolds are reported in Table 1. The uncoated ZrO_2 scaffold total porosity determined by micro-CT (Table 1) was in agreement with that measured by their mass and dimensions (Eq. (1), Fig. 9). The ZrO_2 scaffold total porosity was nearly almost open or interconnected, indicating a negligible pore blocking (Table 1). As reported in several works dealing with scaffolds for bone replacement [29], the achievement of a highly open porous structure is one of the crucial requirements in order to ensure exchange of ions between the scaffold and the surrounding biological environment, migration of cells and tissue formation. A sufficient degree of open porosity is also beneficial for more effective penetration of the bioglass coating along the strut surfaces.

The ZrO_2 scaffold macropore size distribution resulting from micro-CT analysis is presented in Fig. 11a. A wide pore size distribution with pore sizes between 100 and 850 μm was found; a low volume of pores ($<1\%$) with sizes <250 μm was observed. Most of the pores had sizes ranging from 400 to 700 μm and the most frequent pore size was in the range 530–550 μm. The porous structure obtained in this study with large pore sizes and high porosities are expected to be optimum for tissue ingrowth and bone formation.

The strut size distribution of the ZrO_2 scaffold obtained from SEM image analysis is shown in Fig. 11b. The struts had thickness between 30 and 90 μm and the more frequent strut thickness was in the range 50–60 μm. Recent modeling works [30] based on finite element analysis refer to these strut thickness as beneficial for the strength of reticulated ceramics.

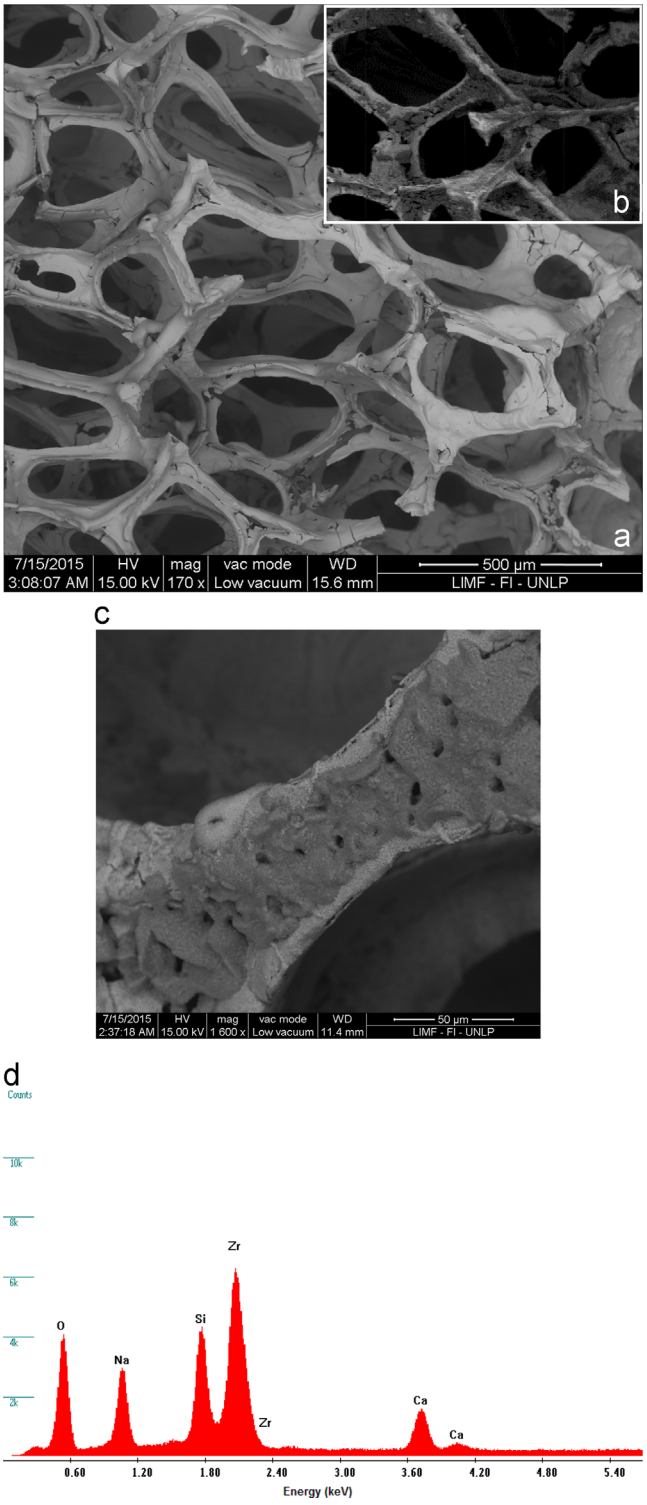

Fig. 10. (a) SEM image of the uncoated ZrO_2 scaffold, (b) SEM image of the coated ZrO_2 scaffold, (c) SEM image (plan view) of a coated strut: glass-ceramic coating (dark phase), ZrO_2 surface (bright phase), (d) EDXA spectrum of the glass-ceramic coating.

More specifically, the stress analysis showed that compression stresses tend to concentrate on the thinner struts. Therefore the optimization of the processing route in order to obtain struts thicker than 20 μm is a desired goal.

Table 1
Porosity values of uncoated and coated ZrO_2 scaffolds obtained with micro-CT.

Porosity	Uncoated ZrO_2 scaffold	Coated ZrO_2 scaffold
Total porosity (%)	87.248	86.098
Open porosity (%)	87.239	86.089
Closed porosity (%)	0.009	0.009

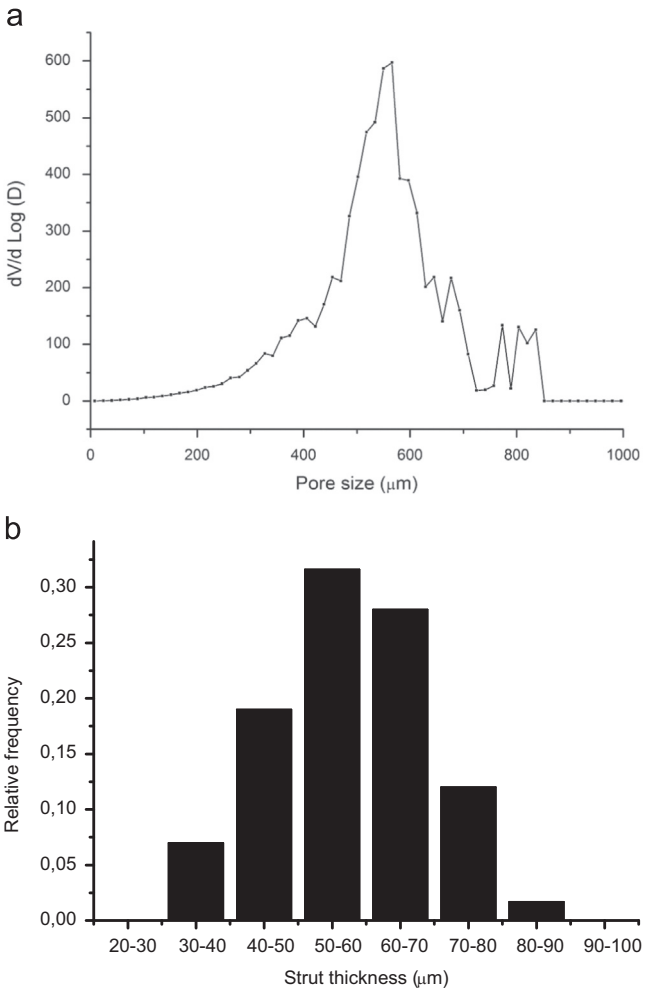

Fig. 11. (a) Macropore size distribution of the uncoated ZrO_2 scaffold, obtained from micro-CT analysis, (b) Strut thickness distribution of the uncoated ZrO_2 scaffold, obtained from SEM image analysis.

The total porosity determined by micro-CT (Table 1) for the coated ZrO_2 scaffolds was in accordance with that measured by their mass and dimensions (Eq. (2)). The increase of weight after coating was about 4 wt%; however, it was possible to observe (Table 1) that the decrease of ZrO_2 scaffold total porosity after the coating procedure was almost negligible (1.15%), indicating an homogeneous distribution of the coating along the strut surfaces. Fig. 10b and c show the microstructure of the coated ZrO_2 scaffold and a coated strut, respectively. The 45S5 bioglass-derived coating (dark phase) along the ZrO_2 strut surface (bright phase) was clearly shown in Fig. 10c. The EDXA spectrum of the coating (Fig. 10d) had sharp signals for O, Na, Si, Ca and Zr; a low intensity signal of O and that of Zr belonged to the ZrO_2 substrate. The 1.75 Kev signal intensity mainly corresponded to Si since the Zr contribution to its intensity is very low.

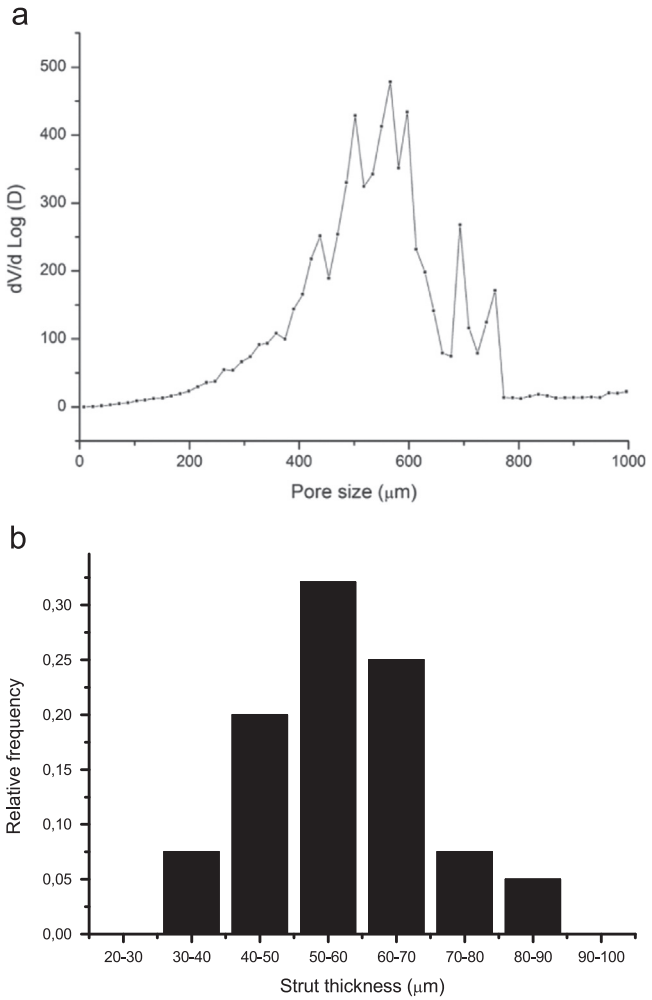

Fig. 12. (a) Macropore size distribution of the coated ZrO_2 scaffold, obtained from micro-CT analysis, (b) Strut thickness distribution of the coated ZrO_2 scaffold, obtained from SEM image analysis.

The sintered layer had some large pores with lengths between 3 and 9 μm (Fig. 10c). The presence of these pores indicated that extensive densification by viscous flow did not occur at 1100 °C, leading to a sintered layer not fully densified. It is generally agreed that micro-and/or nanoporous material surfaces enhance the osteogenic potential of osteoblast cells in vitro, which is ultimately an indication of the materials capacity to promote bone repair in vivo [31].

The well-dispersed 30 wt% 45S5 slip with 4 wt% PVA enabled an effective penetration into the ZrO_2 scaffold resulting in a coating distributed along the strut surfaces (Fig. 10b). At short immersion times, the liquid entrainment mechanism governs the formation of a layer on a porous body during dip coating [32]. The thickness of this layer adhered increases with the withdrawal velocity and the slurry viscosity [32]. As the liquid from the thin layer of slurry evaporates, a thin coating of ceramic particles remains on the surface of the specimen. In the present study, at a constant withdrawal velocity, the low viscosity value of the 45S5 slurry (25.7 mPa.s) produced a thin adhered layer. As it was mentioned in Section 3.1 (Fig. 4),

extensive crystallization occurred prior to 45S5 sintering by viscous flow; and the layer was in fact a glass–ceramic.

The pore size and strut thickness distributions of the coated ZrO_2 scaffolds are presented in Fig. 12a and b, respectively. A similar pore size distribution with respect to the uncoated ZrO_2 scaffold (Fig. 11a) was found. The majority of the pores had sizes between 400 and 770 μm; a high volume of pores with sizes 490, 546 and 583 μm were detected. Nearly the same strut thickness distribution was observed for the uncoated and coated ZrO_2 scaffolds (Figs. 11b and 12b). Thus, the glass–ceramic coating did not affect the whole porous structure of the ZrO_2 scaffolds.

The glass–ceramic coating appeared to be distributed along the strut surfaces, filling the defects and forming a thin film without reducing the porosity or increasing the strut thickness of the original ZrO_2 scaffold structure.

4. Conclusions

Porous ZrO_2 scaffolds coated by glass–ceramic derived from 45S5 bioglass were developed. The surface reactivity and the rheological behavior of 45S5 aqueous slips were investigated. The immersion of 45S5 glass in aqueous solution produced a pH rise from 7.7 to 11.6, which was attributed to the Ca^{2+}, Na^+/H^+ exchange reaction at the glass-solution interface. The high ionic exchange capability of the 45S5 bioglass in an aqueous solution was demonstrated by the increase in pH, the significant weight loss and the amorphous calcium phosphate nucleation, upon its immersion in aqueous solution.

The suspensions were changed from being well stabilized for 20 wt% to weakly flocculated for 30 and 48 wt% solid content. The addition of PVA did not affect the dispersion properties of the 45S5 powder, which were basically controlled by its negative surface charge. 30 wt% 45S5 slips with 4 wt% PVA exhibited a yield stress and an adequate viscosity in the low shear rate range, to produce a bioglass coating into the ZrO_2 scaffold.

ZrO_2 scaffolds produced by foam replication process exhibited 3D interconnected structure with high degree of open porosity. 30 wt% 45S5 slip with 4 wt% PVA having a low viscosity value enabled an effective penetration into the ZrO_2 scaffold, forming a thin glass–ceramic film after thermal treatment, without altering the pore size and the strut thickness of the original ZrO_2 scaffold structure.

Acknowledgment

This work was financially supported by CONICET (2012/Res. D. No 2544), CONICET-PIP0248 and FAPESP 2012/50949-4. The authors are grateful to Adriana Luisa Gonçalves de Almeida for her contribution with the micro-computed tomography analysis.

References

[1] L.L. Hench, The story of Bioglass, J. Mater. Sci. Mater. Med. 17 (2006) 967–978.
[2] J.R. Jones, Review of bioactive glass: From hench to hybrids, Acta Biomater. 9 (2013) 4457–4486.
[3] C. Piconi, G. Maccauro, Zirconia as a biomaterial, Biomaterials 20 (1999) 1–25.
[4] D.W. Hutmacher, Scaffolds in tissue engineering bone and cartilage, Biomaterials 21 (2000) 2529–2543.
[5] K.F. Leong, C.M. Cheah, C.K. Chua, Solid free-form fabrication of three-dimensional scaffolds for engineering replacement tissue and organs, Biomaterials 24 (2003) 2363–2378.
[6] Q.Z. Chen, I.D. Thompson, A.R. Boccaccini, 45S5 Bioglass-derived glass-ceramic scaffolds for bone tissue engineering, Biomaterials 27 (2006) 2414–2425.
[7] J. Cesarano III, Ilhan A. Aksay, Processing of highly concentrated aqueous α-alumina suspensions stabilized with polyelectrolytes, J. Am. Ceram. Soc. 71 (12) (1988) 1062–1067.
[8] H. Guldberg-Pedersen, L. Bergström, Stabilizing ceramic suspensions using anionic polyelectrolytes: adsorption kinetics and interparticle forces, Acta Mater. 48 (2000) 4563–4570.
[9] J.X. Zhang, D.L. Jiang, S.H. Tan., L.H. Gui, M.L. Ruan, Aqueous processing of titanium carbide green sheets, J. Am. Ceram. Soc. 84 (11) (2001) 2537–2541.
[10] A.U. Khan, B.J. Briscoe, P. f Luckham, Interaction of binders with dispersant stabilized alumina suspensions, Colloids Surf. A 161 (2000) 243–257.
[11] F.M. Stábile, C. Volzone, Bioactivity of leucite containing glass–ceramics using natural raw materials, Mater. Res. 17 (2014) 1031–1038.
[12] I. Elgayar, A.E. Aliev, A.R. Boccaccini, A.R. Gill, Structural analysis of bioactive glasses, J. Non -Cryst. Solids 351 (2005) 173–183.
[13] A. Balamurugan, G. Balossier, S. Kannan, J. Michel, A.H.S. Rebelo, J.M. F. Ferreira, Development and in vitro characterization of sol–gel derived $CaO–P_2O_5–SiO_2–ZnO$ bioglass, Acta Biomater. 3 (2007) 255–262.
[14] A. Pedone, T. Charpentier, G. Malavasi, M.C. Menziani, New insights into the atomic structure of 45S5 bioglass by means of solid-state NMR spectroscopy and accurate first principles simulations, Chem. Mater. 22 (2010) 5644–5652.
[15] M. Cerruti, C.I. Bianchi, F. Bonino, A. Damin, A. Perardi, C. Morterra, Surface modifications of bioglass immersed in TRIS-bufferedsolution. A multitechnical spectroscopic study, J. Phys. Chem. B 109 (2005) 14496–14505.
[16] P. Sepulveda, J.R. Jones, L.L. Hench, In vitro dissolution of melt-derived 45S5 and sol–gel derived 58S bioactive glasses, J. Biomed. Mater. Res. 61 (2002) 301–311.
[17] D.S. Brauer, N. Karpukhina, M.D.O. Donnell, R.V. Law, R.G. Hill, Fluoride containing bioactive glasses: effect of glass design and structure on degradation, pH and apatite formation in simulated body fluid, Acta Biomater. 6 (2010) 3275–3282.
[18] C.Y. Kim, A.E. Clark, L.L. Hench, Early stages of calcium-phosphate layer formation in bioglasses, J. Non -Crist. Solids 113 (1989) 195–202.
[19] L.L. Hench, D.E. Ckark, Physical chemistry of glass surfaces, J. Non -Cryst. Solids 28 (1978) 83–105.
[20] M. Cerruti, D. Greenspan, K. Powers, Effect of pH and ionic strength on the reactivity of Bioglass® 45S5, Biomaterials 26 (2005) 1665–1674.
[21] V. FitzGerald, D.M. Pickup, D. Greenspan, D. Sarkar, G. FitzGerald, K. M. Wetherall, A neutron and x-ray diffraction study of bioglass with reverse monte carlo modeling, Adv. Funct. Mater. 17 (2007) 3746–3753.
[22] T. Kokubo, H.-M. Kim, M. Kawashita, Novel bioactive materials with different mechanical properties, Biomaterials 24 (2003) 2161–2175.
[23] L.G. Rodenas, J.M. Palacios, M.C. Apella, P.J. Morando, M.A. Blesa, Surface properties of various powdered hydroxyapatites, J. Colloid Interface Sci. 290 (2005) 145–154.
[24] J. Cesarano III, I.A. Aksay, A. Bleier, Stability of aqueous α-alumina suspensions with poly(methacrylic acid) polyelectrolyte, J. Am. Ceram. Soc. 71 (4) (1988) 250–255.
[25] F.M. Stábile, C. Volzone, Effect of feldspar addition into Bioglass 45S5 composition: Crystallization kinetics and thermal transformation, Glass Physics and Chemistry, Accepted Article.
[26] M.P. Albano, L.B. Garrido, Processing of concentrated aqueous fluor-apatite suspensions by slip casting, J. Mater. Sci. 46 (15) (2011) 5117–5128.

[27] M.P. Albano, L.B. Garrido, A.B. Garcia, Dispersion of aluminium hydroxide coated Si_3N_4 powders with ammonium polyacrylate dispersant, Colloids Surf. A 181 (2001) 69–78.

[28] C.R. Rambo, E. de Sousa, A.P. Novaes de Oliveira, D. Hotza, P. Greil, Processing of cellular glass Ceramics, J. Am. Ceram. Soc. 89 (11) (2006) 3373–3378.

[29] D.M. Yunos, O. Bretcanu, A.R. Boccaccini, Polymer bioceramic composites for tissue engineering scaffolds, J. Mater. Sci. 43 (13) (2008) 4433–4442.

[30] C.D.' Angelo, A. Oriona, P. Colombo, Finite element analysis of reticulated ceramics under compression, Acta Mater. 60 (19) (2012) 6692–6702.

[31] R.A. Gittens, R. Olivares-Navarrete, A. Cheng, D.M. Anderson, T. McLachlan, I. Stephan, J. Geis-Gersorfer, K.H. Sandhage, A. G. Fedorov, F. Rupp, B.D. Boyan, R. Tannenbaum, Z. Schwartz, The roles of titanium surface micro/nanotopography and wettability on the differential response of human osteoblast lineage cells, Acta Biomater. 9 (4) (2013) 6268–6277.

[32] M.G. Pontin, F.F. Lange, A.J. Sánchez-Herencia, R. Moreno, Effect of unfired tape porosity on surface film formation by dip coating, J. Am. Ceram. Soc. 88 (10) (2005) 2945–2948.